Influence of clustering on the magnetic properties and hyperthermia performance of iron oxide nanoparticles

Influence of clustering on the magnetic properties and hyperthermia performance of iron oxide nanoparticles

P Bender[1,*], J Fock[2], M F Hansen[2], L K Bogart[3], P Southern[3], F Ludwig[4], F Wiekhorst[5], W Szczerba[6,7], L J Zeng[8], D Heinke[9], N Gehrke[9], M T Fernández Díaz[10], D González-Alonso[1], J I Espeso[1], J Rodríguez Fernández[1] and C Johansson[11]

[1] Universidad de Cantabria, 39005 Santander, Spain.
[*] Current address: University of Luxembourg, 1511 Luxembourg, Grand Duchy of Luxembourg.
[2] Technical University of Denmark, 2800 Kongens Lyngby, Denmark.
[3] University College London, W1S 4BS London, UK.
[4] Technische Universität Braunschweig, 38106 Braunschweig, Germany.
[5] Physikalisch-Technische Bundesanstalt, 10587 Berlin, Germany.
[6] Bundesanstalt für Materialforschung und -prüfung, 12205 Berlin, Germany.
[7] AGH University of Science and Technology, 30059 Krakow, Poland.
[8] Chalmers University of Technology, 41296 Göteborg, Sweden.
[9] nanoPET Pharma GmbH, 10115 Berlin, Germany.
[10] Institut Laue Langevin, 38042 Grenoble, France.
[11] RISE Acreo, 40014 Göteborg, Sweden.

Abstract. Clustering of magnetic nanoparticles can drastically change their collective magnetic properties, which in turn may influence their performance in technological or biomedical application. Here, we investigate a commercial colloidal dispersion (FeraSpin^{TM}-R), which contains dense clusters of iron oxide cores (mean size around 9 nm according to neutron diffraction) with varying cluster size (about 18 to 56 nm according to small angle X-ray diffraction), and its individual size fractions (FeraSpin^{TM}-XS, S, M, L, XL, XXL). The magnetic properties of the colloids were characterized by isothermal magnetization, as well as frequency-dependent optomagnetic and AC susceptibility measurements. From these measurements we derive the underlying moment and relaxation frequency distributions, respectively. Analysis of the distributions shows that the clustering of the initially superparamagnetic cores leads to remanent magnetic moments within the large clusters. At frequencies below 10^5 rad/s, the relaxation of the clusters is dominated by Brownian (rotation) relaxation. At higher frequencies, where Brownian relaxation is inhibited due to viscous friction, the clusters still show an appreciable magnetic relaxation due to internal moment relaxation within the clusters. As a result of the internal moment relaxation, the colloids with the large clusters (FS-L, XL, XXL) excel in magnetic hyperthermia experiments.

Keywords: magnetic nanoparticles, multi-core particles, core-clusters, magnetic hyperthermia, nanoflowers, numerical inversion

1. Introduction

The collective magnetic properties of magnetic nanoparticle ensembles critically depend on interparticle interactions, which may also significantly influence the performance of the particles in technological or biomedical applications [1, 2]. When particles are introduced in physiological environments, such as cells for example, they often aggregate and form clusters [3, 4]. This induces significant dipolar interactions and is thus a decisive factor for a variety of biomedical applications, in particular magnetic hyperthermia [5].

Magnetic hyperthermia utilizes magnetization reversal losses of nanoparticles in alternating fields to achieve local heating of the surrounding tissue to treat tumors [6, 7]. For small field amplitudes the heating is theoretically either achieved by (i) physical rotation of the whole particle, in case of thermally blocked particles (Brownian relaxation), or by (ii) intrinsic moment fluctuations, in case of superparamagnetic particles (usually described by the Néel-Brown model) [8]. Aggregation of magnetic nanoparticles can thus modify the heating behavior in two ways. First, for thermally blocked particles the physical rotation can be inhibited, which may drastically decrease the dissipated heat by Brownian relaxation [5, 9]. Second, for intrinsically superparamagnetic particles, interparticle interactions (dipolar and/or exchange) may shift the characteristic Néel relaxation times and, as a result, either decrease or increase the performance [10–16].

The observation of an increased heating for some nanoclusters motivated the synthesis of mechanically stable core-clusters, commonly referred to as multi-core particles [17]. A special class of multi-core particles is so-called nanoflowers, in which the cores are so densely packed that they are essentially in direct contact (i.e. nanocrystalline nanoparticles) [14, 18, 19]. The resulting strong interactions between the cores can lead to collective magnetization states within the clusters. The results of several experimental studies indicate that particularly these particle systems excel in magnetic hyperthermia [14–16].

In the current work we have characterized a commercial colloidal dispersion (FeraSpin$^{\text{TM}}$-R), which contains clusters of iron oxide cores with varying cluster size, and its six size fractions (FeraSpin$^{\text{TM}}$-XS, S, M, L, XL, XXL). Their quasi-static and dynamic magnetic properties were determined by isothermal magnetization, optomagnetic and AC susceptibility measurements. From these measurements we extract the underlying moment and relaxation frequency distributions, respectively. Analysis of the distributions, in combination with magnetic hyperthermia experiments, enables us to relate the magnetic structure of the core-clusters with their heat dissipation in alternating fields.

2. Experimental details

2.1. Samples

The seven water-based colloidal dispersions FeraSpin$^{\text{TM}}$-(FS)-R, XS, S, M, L, XL and XXL were supplied by nanoPET Pharma GmbH. FS-R exhibits a broad size distribution and is the mother batch from which the other samples FS-XS→XXL were derived by fractionation [20]. The particles consist of primary core particles with similar size, but which are aggregated to core-clusters with increasing size (XS→XXL) [20–22]. For the AC susceptibility measurements all seven colloids had an iron concentration of 3.7 mg_{Fe}/ml and for the hyperthermia experiments 5 mg_{Fe}/ml. For freeze-drying d-mannitol was added to act as scaffold and thus preventing the particles from agglomeration.

2.2. Methods

From the sample FS-R we took transmission electron microscopy (TEM) images with a FEI Tecnai T20 TEM, using a carbon coated copper grid as sample support.

To determine the size of the iron oxide cores, we analyzed X-ray diffraction (XRD) patterns, which were detected with a Bruker D8 Advance diffractometer, using Cu-Kα radiation ($\lambda = 1.5418$ Å) with a Bragg-Brentano configuration. The freeze-dried samples were placed on a Si single-crystal low background sample holder and the measurements were performed at room-temperature (RT).

Additionally, we conducted a neutron powder-diffraction (ND) experiment on the FS-L freeze-dried sample [23]. The sample was loaded into a vanadium can and data were collected at RT with the high-resolution neutron powder diffractometer D2B at the Institute Laue Langevin with a wavelength of 1.594 Å. Rietveld refinement analyses were performed on both the XRD and the ND data with the FULLPROF Suite [24], using a Thompson-Cox-Hastings pseudo-Voigt profile function to describe the shape of the diffraction peaks.

The total particle (i.e. core-cluster plus surrounding coating) size was deduced from small-angle X-ray scattering (SAXS) measurements of the colloidal dispersions, which were performed with a Kratky system with slit focus, SAXSess by Anton Paar, Graz, Austria. The measurements at RT were obtained in absolute units by subtracting the water and sample holder contributions, and the curves were deconvoluted with the beam profile curve to correct for the slit focus smearing. By performing indirect Fourier transforms (IFTs) of the radially averaged reciprocal scattering intensities $I(q)$, we extracted the underlying real-space pair distance distribution functions $P(r)$ [25–28]. These

distribution functions provide information about the average shape and maximum size of the scatterers in dispersion [29, 30].

The quasi-static magnetic properties of the colloids were investigated by analyzing isothermal DC magnetization (DCM) measurements, which were detected at RT in a Magnetic Property Measurement System (MPMS)-XL (Quantum Design, USA) with applied magnetic fields up to 5 T in logarithmically spaced steps. A volume of 30 μl of the colloids was measured five times and the data points were averaged to determine the measurement uncertainty. The diamagnetic contributions of the empty sample holder and the water were subtracted from the data. The corrected magnetic moment in Am^2 was normalized to the iron mass, which was determined by inductively coupled plasma optical emission spectrometry (ICP-OES), to obtain the magnetization M in units of $\mathrm{Am}^2/\mathrm{kg}_{\mathrm{Fe}}$. From the resulting $M(H)$ curves we derived the underlying apparent moment distributions $P(\mu)$ by numerical inversion [28, 31].

The apparent moment distributions $P(\mu)$ were also extracted from field-dependent optomagnetic ($\mathrm{OM}(H)$) measurements, which were performed at RT in a custom-built cuvette setup described in [32] with low excitation frequencies (in quasiequilibrium). In this setup, the complex even harmonic signal $\tilde{V}_n(\omega) = V_n'(\omega) + iV_n''(\omega)$ (for $n = 0, 2, 4, 6, 8, 12$) in response to a sinusoidal applied magnetic field was found from measured time-traces using FFT. All measurements were normalized by the sum of even harmonics, $V_{\mathrm{ref}} = \sum_{i=0}^{6} V_{2i}$, to correct for any possible variations in the intensity of incoming light.

Moreover, analysis of OM measurements obtained as function of field *and* frequency dependent ($\mathrm{OM}(H, \omega)$) were used to estimate the bivariate lognormal distribution of magnetic moments and relaxation frequencies including their correlation for the particle ensemble [33]. The distribution of relaxation frequencies $P(\omega_c)$ could be extracted from this distribution to enable comparison to other methods.

The relaxation dynamics of the colloids at RT was also determined by frequency-dependent AC susceptibility (ACS) measurements. The complex volume susceptibility $\chi(\omega) = \chi'(\omega) + i\chi''(\omega)$ was measured with a custom-built setup described in [34], which uses an field amplitude of 95 μT, following the protocol described in [20]. By a numerical inversion of the ACS spectra we derived $P(\omega_c)$ [31, 35]. The uncertainty was not known and we assumed for each data point a reasonable value of $\sigma = 0.05 \cdot \chi'_{\mathrm{max}}$.

Magnetic hyperthermia measurements were performed using a magnetic alternating current hyperthermia 'MACH' system (Resonant Circuits Ltd, UK) following a previously described sample preparation and ILP analysis method [36]. The applied alternating uniaxial field had an amplitude of $\mu_0 H = 8.8\,\mathrm{mT}$ and an angular frequency of $\omega = 5.9 \cdot 10^6\,\mathrm{rad/s}$.

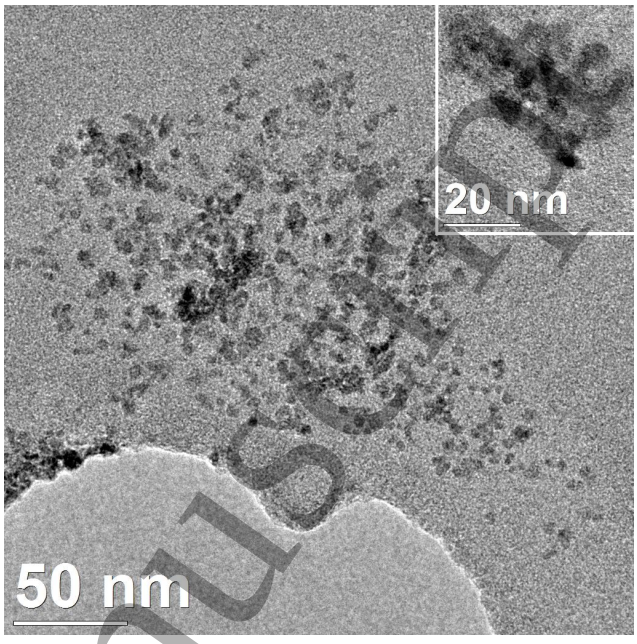

Figure 1. TEM image of the sample FS-R (mother batch) from which the six size fractions FS-XS, S, M, L, XL and XXL were derived. *inset*: Typical cluster found in FS-L.

3. Results

3.1. TEM

Figure 1 shows a representative TEM image of FS-R. As can be seen, the cores are quite irregular in shape and partially aggregated to clusters with varying size, although quite many of the cores seem to be dispersed individually. The *inset* of figure 1 displays a typical cluster of the sample FS-L. A more detailed TEM analysis of the individual cores (sample FS-XS) and of the sample FS-L can be found in [21], where the authors found the mean core size to be around 6 nm and a quite broad distribution of the core-cluster size. In this work we use XRD and ND to estimate the mean core size, and SAXS to determine the average core-cluster size of the individual size fractions.

3.2. XRD and ND results

Figure 2 contains the XRD and the ND pattern of the FS-L sample. The XRD patterns of the FS-XS and R sample are shown in figure A1 and the results of the Rietveld refinements are given in table A1 in the appendix.

In the XRD patterns, two groups of peaks having different widths can immediately be distinguished.

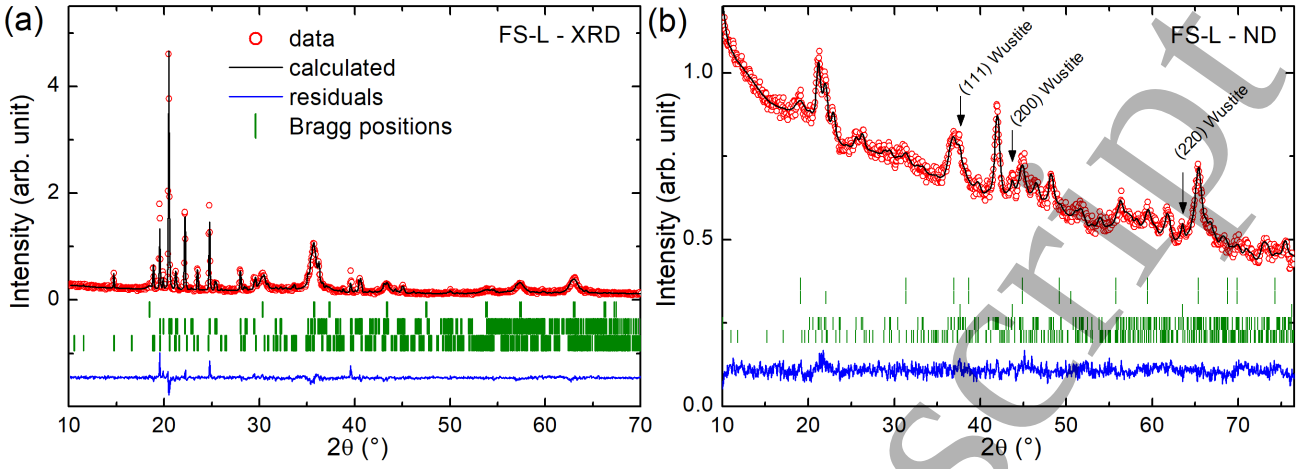

Figure 2. Rietveld refined (a) XRD pattern ($\lambda = 1.5418$ Å) of FS-L, and (b) the ND pattern ($\lambda = 1.594$ Å) of FS-L (all measured at RT). Vertical tick marks in panel (a) indicate the positions of the diffraction peaks of three refined phases, which are from bottom to top (1) β and (2) δ D-mannitol, as well as (3) a mixture of magnetite/maghemite phases in the $Fd\bar{3}m$ space group. In panel (b) the arrows indicate the peaks corresponding to wüstite. The vertical marks indicate the positions of the diffraction peaks of 5 refined phases, which are from bottom to top (1) β and (2) δ D-mannitol (nuclear), (3) wüstite (nuclear), and both (4) magnetic and (5) nuclear contributions of the mixture magnetite/maghemite phase.

The sharper peaks found at low angles correspond to the β and δ polymorphs of the acyclic sugar alcohol D-mannitol [37], which was used to prevent agglomeration during the freeze-drying. In the samples we have discriminated the β and δ polymorphs of D-mannitol, which crystallize in the orthorhombic $P2_12_12_1$ and monoclinic $P2_1$ space groups, respectively. The derived lattice parameters agree well with those reported in [37]. The broader diffraction peaks arise from the iron oxide core phase. All reflections can be indexed with a cubic $Fd\bar{3}m$ space group with a lattice parameter $a \approx 8.36$ Å(see table A1 for details). This value of the lattice parameter suggests that the iron oxide phase must be a mixture of maghemite (γ-Fe_2O_3) for which $a \cong 8.34$ Å [38, 39] and magnetite (Fe_3O_4) for which $a \cong 8.39$ Å [40]. The average derived crystallite/core sizes are 7(2) nm for FS-XS and R, and 11(4) nm for FS-L; but it should be noted that the XRD patterns indicate that the samples were textured.

Figure 2(b) presents the refined ND pattern of the FS-L sample. The pattern exhibits less texture than the XRD pattern, which we explain by the higher penetration depth of neutrons compared to X-rays. Analysis of the ND pattern reveals a minor weight fraction of about 2 wt% of wüstite, which is another iron oxide phase with a $Fm\bar{3}m$ space group [41]. The diffraction peaks of wüstite are marked by arrows in figure 2(b). A magnetic contribution of wüstite to the ND pattern was not considered because its magnetic ordering temperature is below 200 K [42]. The refined core size is 9(4) nm. Considering the large uncertainties on the core sizes derived from XRD and ND, and the texture observed by XRD, we estimate a mean core diameter for all samples of around 9 nm (7-11 nm). In [21] the mean core size was estimated *via* TEM to be a around only 6 nm. We attribute this discrepancy to the different weightings of the techniques. Whereas, the mean size derived from TEM is the number weighted mean, the mean core size determined with XRD and ND is intensity weighted, which naturally results in larger values. It can be noted, that the estimated value of around 9 nm for the mean core size agrees well with the results from SAXS, which is shown in the following subsection.

3.3. SAXS

Figure 3(a) shows the radially averaged SAXS intensities $I(q)$ of the seven colloids and figure 3(b) the derived pair distance distribution functions $P(r)$. The detected maximum size of the core-clusters (when $P(r)$ reaches zero) increases systematically from 18 nm (XS) to 56 nm (XXL and R).

The distribution of FS-XS has a maximum at around 4.5 nm, which agrees well with the $P(r)$ function calculated for a sphere with a diameter of 9 nm (dotted line in figure 3(b)) [28, 30]. This additionally confirms that the individual cores are around 9 nm in size, although it has to be considered that with SAXS also the surrounding coating is detected, which increases the total particle size. The determined maximum size, though, is 18 nm and the elongated shape of $P(r)$ then indicates that at least some of the cores were aggregated to dimers.

The distributions of the larger size fractions are systematically shifted to higher values, but without a significant change in shape compared to FS-XS. These

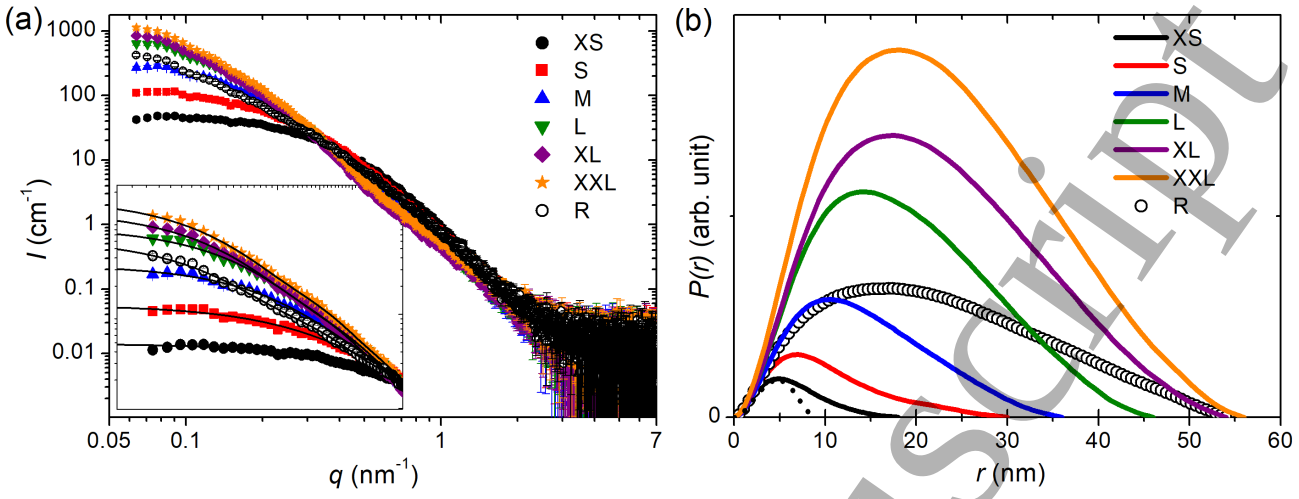

Figure 3. (a) Radially averaged SAXS intensities $I(q)$ of the colloids with measurement uncertainties. The inset shows the low q-range, where the solid lines are the fits by IFTs. (b) Pair distance distribution functions $P(r)$ determined by IFTs of $I(q)$. The dotted line represents the $P(r)$ function calculated for a homogeneous sphere with a diameter of 9 nm.

observations verify that the samples FS-XS→XXL contain in fact distinct fractions of core-clusters with systematically increasing size. Considering that for isometric clusters we would expect a bell-like shape of $P(r)$, the elongated shape of the experimentally determined distributions for all seven samples suggests that the clusters tend to be anisotropic, as also observed by electron microscopy in [21].

3.4. DCM measurements

In figure 4(a) the DCM curves $M(H)$ of the seven colloids are plotted. The detected magnetization at $\mu_0 H = 5\,\mathrm{T}$ ($H = 3.2 \cdot 10^6\,\mathrm{A/m}$) varies between $80 - 100\,\mathrm{Am^2/kg_{Fe}}$. Assuming the stoichiometry of maghemite, this corresponds to a volume magnetization of around $2.7 \cdot 10^5 - 3.4 \cdot 10^5\,\mathrm{A/m}$, which is below the literature value for the saturation magnetization of maghemite ($4 \cdot 10^5\,\mathrm{A/m}$) [43]. This suggests a certain amount of uncorrelated spins within the particles.

Figure 4(b) shows the $M(H)$ data for the FS-R sample along with the weighted superposition of the $M(H)$ curves of the individual fractions. The weighting factors $c_{\mathrm{XS}\rightarrow\mathrm{XXL}}$ were determined by a least-square fit and can be interpreted as the relative volume fractions. As expected, the weighted superposition of the size fractions provides an accurate representation of the data for the FS-R sample.

From the individual DCM curves of all seven samples, we derived the apparent magnetic moment distributions $P(\mu) = M_S p(\mu) \Delta\mu$ plotted in figure 4(c). Here, $p(\mu)$ is the moment-weighted probability density and $\Delta\mu$ was logarithmically spaced ($\sum p(\mu)\Delta\mu = 1$).

The apparent magnetic moment distribution of the FS-XS size fraction was well described by a broad number-weighted lognormal distribution with $\sigma = 1.1$ and a mean moment of $\langle\mu\rangle = 3.6 \cdot 10^{-20}\,\mathrm{Am^2}$, as shown in figure 4(c) (grey area; in the plot, the distribution was transformed to a moment-weighted distribution and weighted by logarithmically spaced $\Delta\mu$, thus resulting in a moment square weighted distribution). From the mean magnetic moment we can estimate the effective magnetic core size D_m. With $M_S = 2.7 \cdot 10^5\,\mathrm{A/m}$ and assuming spherical shape (i.e. $\mu = \pi M_S D_m^3/6$) we obtain $D_m \approx 6.3\,\mathrm{nm}$, which is smaller than but close to the diameter of the individual cores determined by XRD and ND. This indicates that the moment distribution determined for FS-XS corresponds to the intrinsic moment distribution of the individual cores, where the slightly reduced magnetic core diameter may be due to uncorrelated surface spins [44–46] or an internal spin disorder [45, 46].

For the fractions S→XXL, a clearly bimodal distribution emerged (figure 4(c)). The peak in the low-moment range is for all samples at about the same position as the distribution of FS-XS, which can be thus interpreted as a signature of the primary cores. The main peak in the high-moment range, attributed to clusters, was shifted to higher values for increasing size fractions. This shows that the larger clusters have higher effective magnetic moments. The largest effective moments are accordingly detected for the samples FS-L, XL and XXL, with average values of roughly $2{\cdot}10^{-18}\,\mathrm{Am^2}$, $2.5{\cdot}10^{-18}\,\mathrm{Am^2}$ and $3{\cdot}10^{-18}\,\mathrm{Am^2}$, respectively.

In figure 4(d) we show that the weighted superposition of the distributions of the individual fractions results in the same bimodal distribution as determined for the mother batch FS-R. This verifies the existence of the two aforementioned distinct

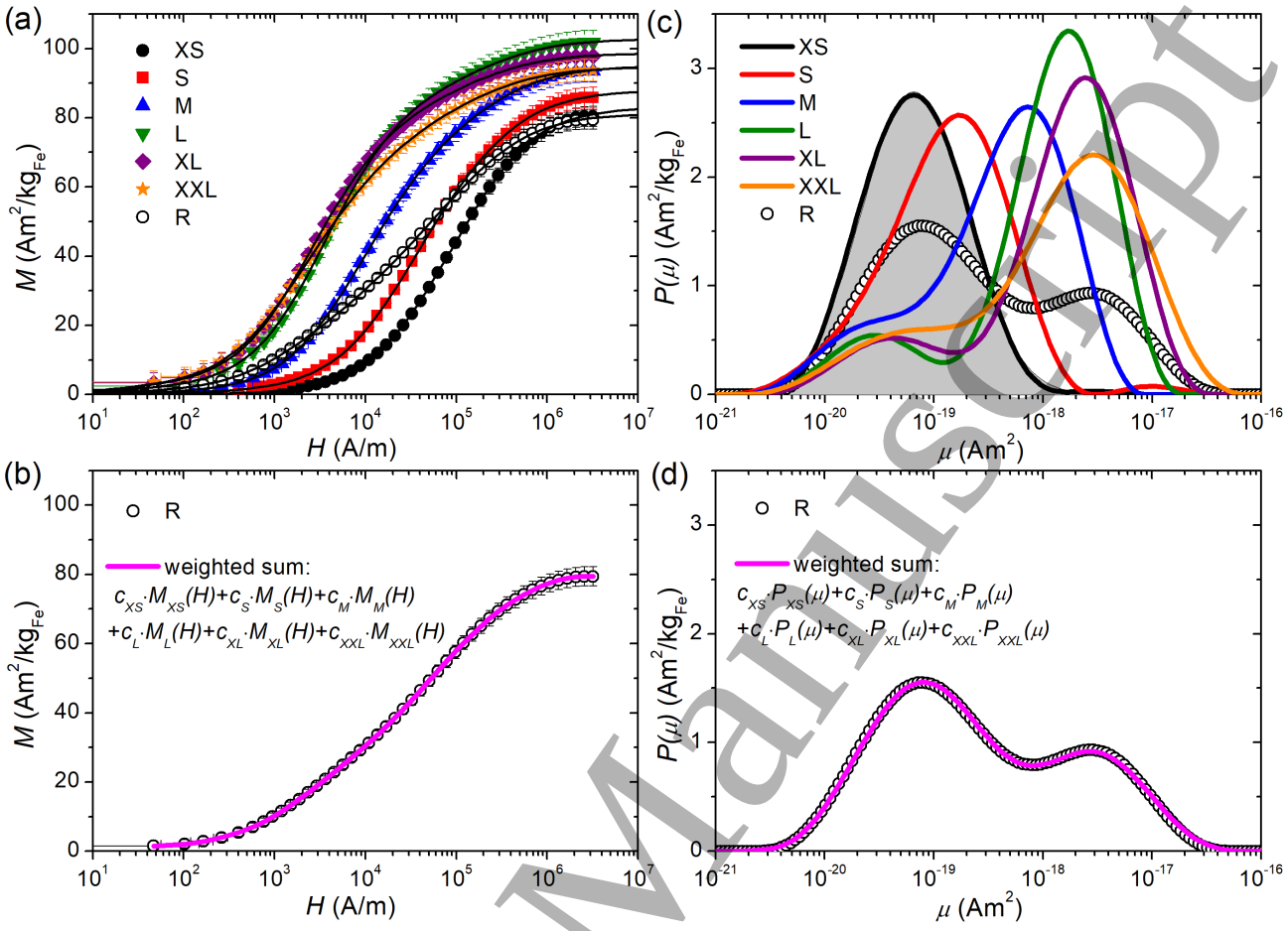

Figure 4. (a) DCM measurements $M(H)$ of the colloids with measurement uncertainties. Continuous lines are the fits by numerical inversion. (b) $M(H)$ measurement of the mother batch FS-R. Continuous (magenta) line is the weighted superposition of the $M(H)$ curves of the individual fractions FS-XS→XXL with $c_{\mathrm{XS}} = 0.374$, $c_{\mathrm{S}} = 0.144$, $c_{\mathrm{M}} = 0.006$, $c_{\mathrm{L}} = 0.005$, $c_{\mathrm{XL}} = 0.070$, $c_{\mathrm{XXL}} = 0.313$. These values were determined by a least-square fit. (c) Discrete moment-weighted apparent moment distributions $P(\mu) = M_{\mathrm{S}} p(\mu) \Delta\mu$ of the colloids determined by numerical inversion of the $M(H)$ curves. Grey area is the transformed and rescaled distribution calculated for a number-weighted lognormal distribution $p(\mu)$ with $\sigma = 1.1$ and a mean value of $\langle\mu\rangle = 3.6 \cdot 10^{-20}\,\mathrm{Am}^2$. (d) $P(\mu)$ of the mother batch FS-R. Continuous (magenta) line is the weighted superposition of the $P(\mu)$ distributions of the individual fractions FS-XS→XXL. As weighting factors $c_{\mathrm{XS}\to\mathrm{XXL}}$ we used the values determined from the superposition of DCM curves shown above.

moment regimes, corresponding to the individual cores (peak in low-moment range) and the effective moments of the core-clusters (peak in high-moment range).

3.5. OM measurements

OM measurements probe the physical orientations of anisometric magnetic nanoparticles. The signal is weighted by the extinction properties of the magnetic nanoparticles and therefore by their volume, which in case of single-cores is directly proportional to their moment [32]. Figure 5(a) shows the even harmonics ($n = 2, ..., 12$) of the quasiequilibrium OM(H) response for field amplitudes up to $\mu_0 H = 0.23\,\mathrm{T}$ for the FS-XS sample. The measurements deviate only little from the quadratic response (linear in double-log plot) expected for very small moments, and a fitted moment distribution $P(\mu)$ will therefore not be well determined. Instead the data was analyzed using a lognormal distribution with the moment-weighted median value obtained from DCM measurements resulting in $\sigma = 1.29$. Assuming that FS-XS primarily consists of single core particles, the moment is proportional to the particle volume and the intrinsic weighting of the OM signal is consequently moment weighted. The moment distribution in figure 5(a) (black curve) was converted to be weighted by the moment square to enable a direct comparison to the moment distribution obtained from $M(H)$ measurements (red curve). The two distributions are found to be in good agreement.

For the larger fractions FS-S→XXL and FS-R, a superposition of two lognormal distributions was needed to fit the OM(H) measurements, where one

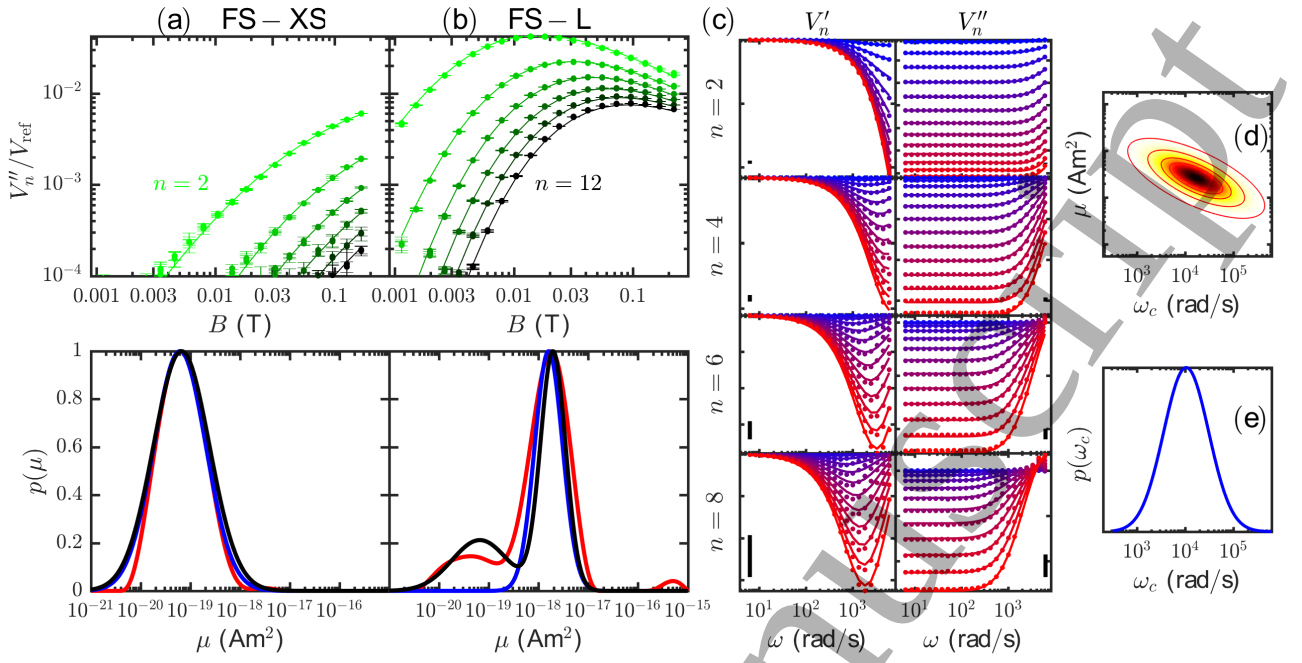

Figure 5. OM(H) measurements at low frequency of (a) FS-XS and (b) FS-L. *Top:* Lines from green to black are increasing even harmonics from 2 to 12. *Bottom:* Red curves are the distributions derived by numerical inversion of the DCM measurements, and black curves are the distributions obtained by fitting the OM(H) measurements assuming a superposition of two lognormal functions for $P(\mu)$. The blue curve for FS-L is the unimodal lognormal distribution determined by fitting the OM(H, ω) measurements, which were performed at low field amplitudes (large moments are dominating the signal). All plotted distributions are moment square weighted. (c) OM(H, ω) response (V_n' and V_n'') of FS-L. The colors are from blue to red $\mu_0 H = 0.5$ mT to $\mu_0 H = 6.5$ mT in steps of 0.5 mT. The lines are from the global fit using a bivariate lognormal distribution shown in (d). (e) Determined unimodal lognormal distribution of characteristic (Brownian) relaxation frequencies of FS-L, weighted with the extinction properties.

distribution had parameters (except for scaling) fixed to the values obtained for the FS-XS sample and the other lognormal distribution was free to vary. The first distribution is used to generally represent low magnetic moments and it should be noted that these, due to the weighting of the OM signal, contribute only little to the total signal. Figure 5(b) shows the data and moment distribution for FS-L. The determined distribution (black curve) was found to be in good agreement with the bimodal distribution derived from the DCM data.

The samples where also characterized by OM(H, ω) measurements. The experiments were performed with $\mu_0 H \leq 6.5$ mT where the signal was dominated by the high-moment peak of the bimodal moment distribution, which was attributed to the clusters. Figure 5(c) shows the real part, V_n', and the imaginary part, V_n'', of the first four even harmonics of the OM signal. The spectra for all investigated harmonics were analyzed simultaneously in terms of a unimodal bivariate lognormal distribution of moments and Brownian relaxation frequencies, which also included the correlation between these two parameters [33]. The inclusion of the higher harmonics in the analysis enabled determination of the Brownian frequency distribution even when the peak of V_2' was outside the measurement window as spectral features are shifted to lower frequencies in the higher harmonics.

The obtained distribution, shown in figure 5(d), displays a correlation between the moment and Brownian relaxation frequency, which can be described by $\mu \propto \omega_c^{-0.49}$. As $1/\omega_c \propto V$, we therefore approximately find that $\mu \propto V_{\rm h}^{0.5}$, which is expected for multi-core particles with randomly oriented magnetic moments [47].

The unimodal moment distribution obtained from the analysis of the OM(H, ω) data at comparatively low field strengths is in good agreement with the high-moment peak of the bimodal distribution extracted from the OM(H) and DCM measurements performed at higher field strengths (figure 5(b)). We recall that this peak describes the effective moments of multi-core particles and that the peak at $\mu \simeq 10^{-20}$ Am^2 in figure 5(a,b) is due to single cores.

Similar analyses were performed for the other fractions (shown in the appendix, figure A2). The results allowed us to divide the individual sample fractions into three groups:

(i) The FS-XS sample consisted mostly of the individually dispersed single-cores and a fraction of small clusters of cores (e.g. dimers). We assume that the signal is dominated by single-cores.

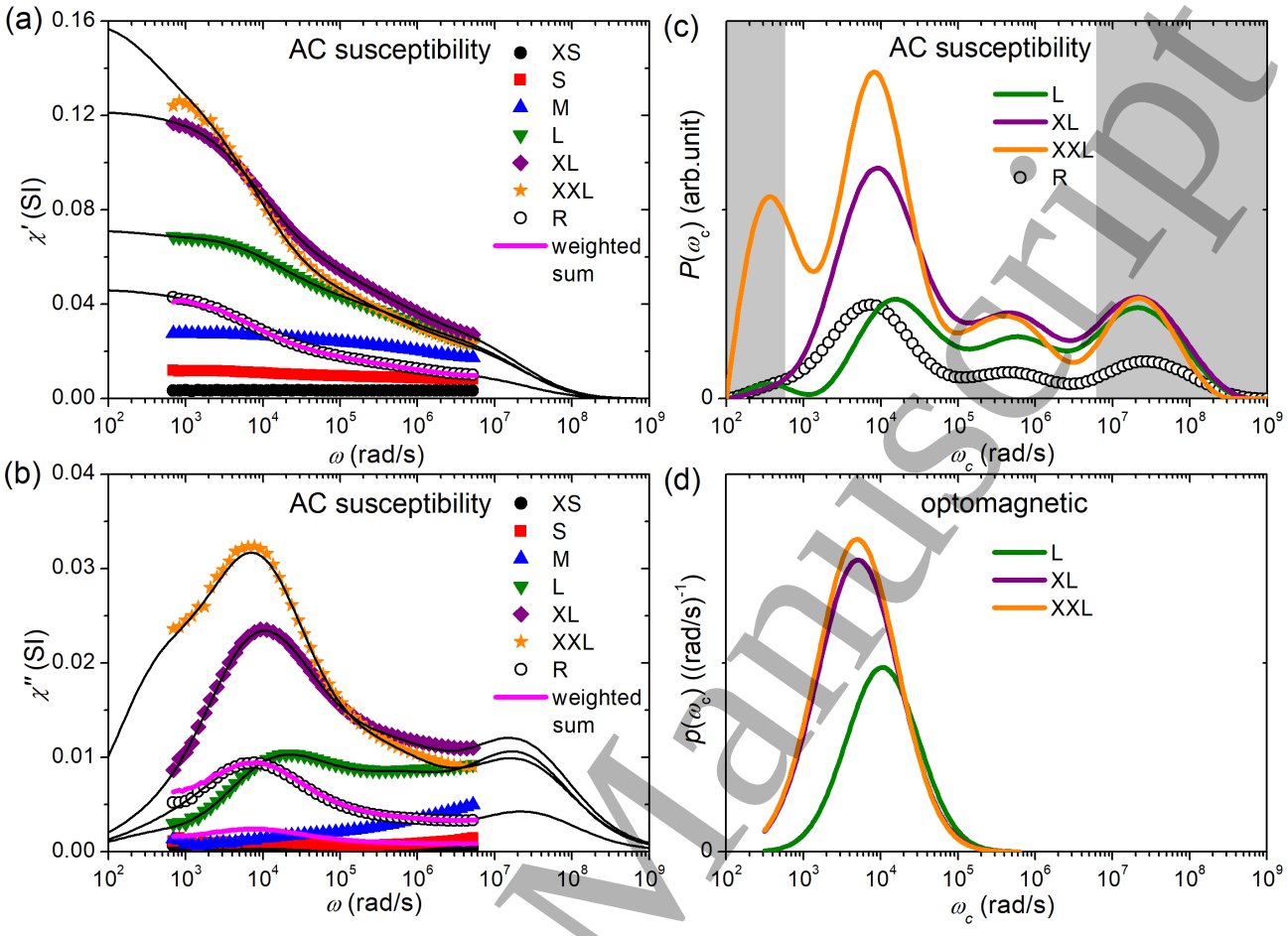

Figure 6. (a) Real and (b) imaginary part of the volume susceptibility $\chi(\omega) = \chi'(\omega) + i\chi''(\omega)$ of the colloids (every second data point shown). The weighted sum $c_{\mathrm{XS}} \cdot \chi_{\mathrm{XS}}(\omega) + c_{\mathrm{S}} \cdot \chi_{\mathrm{S}}(\omega) + c_{\mathrm{M}} \cdot \chi_{\mathrm{M}}(\omega) + c_{\mathrm{L}} \cdot \chi_{\mathrm{L}}(\omega) + c_{\mathrm{XL}} \cdot \chi_{\mathrm{XL}}(\omega) + c_{\mathrm{XXL}} \cdot \chi_{\mathrm{XXL}}(\omega)$ was calculated using the weighting factors derived from the DCM measurements. Continuous lines for L, XL, XXL and R are the fits by numerical inversion. (c) The characteristic relaxation frequency distributions $P(\omega_c)$ derived by numerical inversion of the ACS measurements. For the inversion we assumed for each data point an uncertainty of $0.05 \cdot \chi'_{\max}$. The grey area indicates the frequencies outside the experimentally accessible range. (d) Unimodal lognormal distributions $p(\omega_c)$ of the three samples FS-L, XL and XXL determined by fitting the $\mathrm{OM}(H, \omega)$ data.

(ii) The FS-S and partly also the FS-M samples consisted of a mixture of single-cores, small clusters and slightly larger multi-core particles. The OM signal was dominated by the larger multi-core particles, but the contributions from smaller clusters and single-cores were not negligible. The analysis of the $\mathrm{OM}(H, \omega)$ data in figure A2(a) was therefore representing the multi-core particles with a small influence from single-cores. This made the exponents relating the moment and hydrodynamic size determined from the unimodal fit less reliable.

(iii) The FS-L→XXL samples were dominated by large multi-core particles. It is noted that the low-moment peak in figure A2(b) obtained from $\mathrm{OM}(H)$ measurements had a fixed shape and thus was an effective representation of the signal due to low-moment particles (single-cores or small clusters of single-cores). Although the peak appears large in the distribution, it represents only a very small correction to the signal from the large multi-core particles as the field alignment is small for small moments. Therefore, the contribution from these particles to the $\mathrm{OM}(H, \omega)$ measurements at low fields was negligible and the measurements could be taken as representative for the large multi-core particles. From the unimodal analysis of the $\mathrm{OM}(H, \omega)$ data we found for all samples that the clusters had approximately $\mu \propto V_{\mathrm{h}}^{0.5}$.

3.6. ACS and magnetic hyperthermia experiments

The real and imaginary parts of the volume susceptibilities $\chi(\omega) = \chi'(\omega) + i\chi''(\omega)$, measured for all seven colloids, are depicted in figure 6(a) and (b), respectively. Additionally, we show in both panels the weighted superposition of the curves of the individual fractions FS-XS→XXL, for which we used the weighting factors de-

termined from isothermal magnetometry. Again, the superposition is in good agreement with the measured susceptibility of the mother batch R.

For the smaller fractions FS-XS, S and M we observe a monotonic decrease of the real part, and a monotonic increase of the imaginary part. This indicates that most relaxation processes occur outside the accessible frequency range. We explain this by the dominance of Néel-like relaxation processes of the moments of the primary core particles, for which the characteristic relaxation frequencies are above $\omega_{\max} = 5.7 \cdot 10^6\,\mathrm{rad/s}$. However, for the three large fractions L, XL, XXL as well as the mother batch R, which solely contain core-clusters, a distinct relaxation peak at around $\omega_{\max} = 10^4\,\mathrm{rad/s}$ is observed in the imaginary part (figure 6(b)).

Accordingly, the derived discrete relaxation time distributions $P(\omega_c) = p(\omega_c)\Delta\omega_c$ each exhibit a pronounced peak in this frequency region (figure 6(c)). Here, $p(\omega_c)$ is the moment-weighted probability density distribution and $\Delta\omega_c$ is logarithmically spaced. These peaks (grey area in figure 6(c)) are in good agreement with the unimodal lognormal distributions $p(\omega_c)$ obtained from the combined fit of the $\mathrm{OM}(H,\omega)$ data (figure 6(d)). Only physical particle rotation can be detected with OM measurements and hence the distributions correspond to the distributions of Brownian relaxation times, with $\tau_c = 1/\omega_c = 3\eta V_h/(k_B T)$, where η is the viscosity, V_h is the hydrodynamic volume and $k_B T$ is the thermal energy. In turn, this also means that the additional contributions in the high-frequency range, which we observe by the ACS measurements, have to be due to internal Néel-like relaxation processes. It should be mentioned that the detailed features in the distribution of relaxation times obtained by numerical inversion near and outside the ACS measurement frequency range ($\omega < \omega_{\max} = 5.7 \cdot 10^6\,\mathrm{rad/s}$) in figure 6(c) are likely to be numerical artifacts and should thus not be interpreted in detail. Also it should be noted that the additional peak observed for FS-XXL at very low frequencies can be probably attributed to a partial particle agglomeration in the sample.

Despite the missing information in the high-frequency range, we can surmise from the finite values of χ'' at the highest measurement frequency $\omega_{\max}$ for the three samples FS-L, XL, XXL a considerable internal moment relaxation within the core-clusters. The values of χ'' measured at $\omega_{\max}$ for all samples are listed in table 1. Within the linear response theory the generated heat during hyperthermia experiments is directly proportional to χ'', and the so-called intrinsic loss power (ILP) is given by $(\mathrm{ILP})_{\mathrm{calc}} = (\pi\mu_0/c_{\mathrm{Fe}}) \cdot \chi''$, where $\mu_0 = 4\pi \cdot 10^{-7}\,\mathrm{Vs/(Am)}$ is the permeability of free space and c_{Fe} is the iron mass concentration

Table 1. Imaginary part χ'' of the volume susceptibility of the seven colloids measured at $\omega_{\max} = 5.7 \cdot 10^6\,\mathrm{rad/s}$ (figure 6), the estimated values for the intrinsic loss power $(\mathrm{ILP})_{\mathrm{calc}} = (\pi\mu_0/c_{\mathrm{Fe}}) \cdot \chi''(\omega_{\max}) = 1.1 \cdot 10^3 \cdot \chi''(\omega_{\max})\,\mathrm{nHm^2/kg_{Fe}}$ and the measured values $(\mathrm{ILP})_{\mathrm{meas}}$.

Sample	$\chi''(\omega_{\max})$ (SI)	$(\mathrm{ILP})_{\mathrm{calc}}$ ($\mathrm{nHm^2/kg_{Fe}}$)	$(\mathrm{ILP})_{\mathrm{meas}}$ ($\mathrm{nHm^2/kg_{Fe}}$)
FS-XS	$0.43 \cdot 10^{-3}$	0.472	0.14 ± 0.09
FS-S	$1.52 \cdot 10^{-3}$	1.673	0.98 ± 0.17
FS-M	$5.11 \cdot 10^{-3}$	5.620	2.46 ± 0.16
FS-L	$9.36 \cdot 10^{-3}$	10.296	4.64 ± 0.18
FS-XL	$11.08 \cdot 10^{-3}$	12.184	4.96 ± 0.16
FS-XXL	$9.05 \cdot 10^{-3}$	9.953	4.76 ± 0.13
FS-R	$3.39 \cdot 10^{-3}$	3.732	2.17 ± 0.15

[8, 36]. For the ACS measurements the seven colloids had an iron concentration of $c_{\mathrm{Fe}} \approx 3.7\,\mathrm{mg_{Fe}/ml}$ [20]. Hence $(\pi\mu_0/c_{\mathrm{Fe}}) = 1.1 \cdot 10^3\,\mathrm{nHm^2/kg_{Fe}}$, and within the linear response theory, the values for the ILP can be calculated (table 1). Table 1 additionally reports the measured values, $(\mathrm{ILP})_{\mathrm{meas}}$. A comparison of the calculated and measured ILP values reveals that the measured values are systematically lower. A linear fit of $(\mathrm{ILP})_{\mathrm{calc}}$ vs. $(\mathrm{ILP})_{\mathrm{meas}}$ results in a slope of 2.3(1).

This shift can be attributed to a non-linear magnetization behavior, considering that the ACS measurements were performed with an amplitude of the excitation field of $95\,\mu\mathrm{T}$ and the ILP measurement with an amplitude of 8.8 mT. Despite this discrepancy, the two ILP values are qualitatively in good agreement. This is confirmed by the Pearson correlation coefficient between the two data sets of $R = 0.99$. This coefficient is a measure of the linear correlation between the two data sets, where a $R = 1$ would imply a perfect linear relationship. Thus, the hyperthermia experiments show that the samples FS-L, XL and XXL, which contain the largest clusters of the intrinsically superparamagnetic cores, are the best heaters. Moreover, the ILP values measured for these samples compare favorably to those obtained for other iron oxide nanoparticle samples in the literature where typical values in the range 0.2-4.4 $\mathrm{nHm^2/kg_{Fe}}$ have been reported [48].

Comparing the present samples to the nanoflowers studied in [35], subtle differences are observed. The nanoflowers were found to consist of intergrown seeds with a clear overlap but slightly varying orientations. Consequently they were considered as particles with a nanocrystalline slightly disordered substructure. The magnetic moment of a particle was found to be roughly proportional to the particle volume indicating a preferentially ferromagnetic coupling between the subcomponents of a particle. The particles in

the present study were formed by clustering of well-defined cores that were not intergrown but form dense structures via oriented attachment [21]. Considering the dipole interaction between two cores separated by a particle diameter (9 nm) and with the magnetic moment μ found from DCM measurements, we estimate an interaction energy on the order of $\mu_0\mu^2/k_\mathrm{B} \approx 150\,\mathrm{K}$, which is sufficiently high to significantly influence the magnetic dynamics at room temperature. In addition, cores in contact may also couple by exchange interactions and this coupling could be significant, but less so compared to the nanoflowers studied in [35]. The nature of the exchange coupling can be ferromagnetic (direct exchange), antiferromagnetic (superexchange) or a mixture thereof depending on the atomic sites in contact. However, the relative importance of dipole and exchange interactions is not easily disentangled. We observe that the interactions between the cores in the clusters result in a non-zero remanent moment and that this moment in the large clusters is proportional to the squareroot of the particle size as expected for multi-core particles with randomly oriented thermally blocked core moments. This suggests that the core moments are oriented at random and that the relaxation of the otherwise superparamagnetic single cores is slowed down and broadened over a wide frequency range by the interactions between the cores.

4. Conclusions

We analyzed the magnetic properties and hyperthermia performance of a commercial sample named FeraSpin$^{\mathrm{TM}}$-(FS)-R. FS-R consists of iron oxide cores, which are partially aggregated to clusters with a broad distribution of the cluster size. Additionally, we investigated the six samples FS-XS, S, M, L, XL and XXL, which were obtained by a fractionation of the mother batch FS-R. According to XRD and ND the primary iron oxide cores have a size of about 9 nm, and SAXS confirmed that the average size of the core-clusters within the samples FS-XS→XXL systematically increases from 18 nm (XS)→56 nm (XXL).

The isothermal and dynamic magnetic properties of the seven samples were characterized by DCM, and frequency-dependent OM as well as ACS measurements. From these data sets we derived the underlying discrete moment and relaxation frequency distributions, respectively. The extracted distribution functions showed (i) that the cores are intrinsically superparamagnetic with high characteristic relaxation frequencies and (ii) that the clusters have large induced remanent moments. As a result, these clusters tend to align by Brownian rotation in case of alternating fields with low excitation frequencies. For high excitation frequencies comparison of the OM and ACS results revealed that the Brownian rotation is inhibited due to viscous friction. Nevertheless, the samples with large clusters (FS-L, XL, XXL) maintained a significant out-of-phase susceptibility up to the highest measurement frequencies. This relaxation dynamics could consequently be attributed to Néel-like relaxation of the core moments within the cluster. Finally, we showed that this relaxation observed for the samples with large clusters correlated with superior performance in magnetic hyperthermia experiments.

Acknowledgments

We acknowledge the Institut Laue Langevin for provision of beamtime at the instrument D2B. This project (NanoMag) has received funding from the European Commission Framework Programme 7 under grant agreement no 604448.

Appendix

Additional XRD and ND results

Figure A1 shows the refined XRD patterns of the samples FS-XS and R, and table A1 lists the main parameters obtained from the Rietveld refinement of all XRD and ND patterns

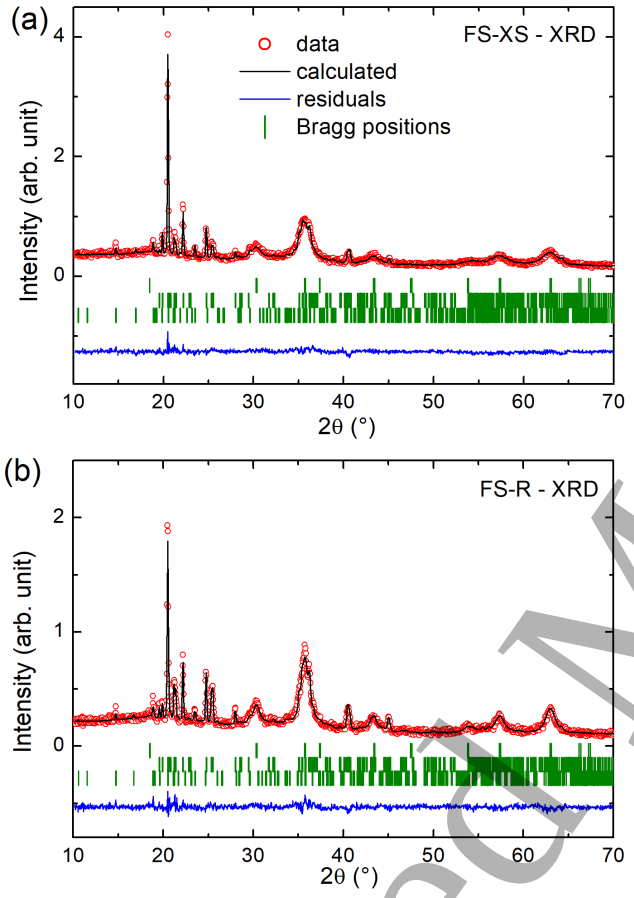

Figure A1. Rietveld refined XRD patterns ($\lambda = 1.541$ Å) of (a) FS-XS, (b) FS-R. Vertical tick marks indicate the positions of the diffraction peaks of three phases (from bottom to top) (1) β and (2) δ D-mannitol, as well as (3) a mixture of magnetite/maghemite phases in the $Fd\bar{3}m$ space group.

Additional OM results

In figure A2(a) we plot the bivariate lognormal distribution obtained from fits to the OM(H, ω) data of all seven samples, and in figure A2(b) we compare the apparent moment distributions determined from the OM measurements with the distributions derived from the DCM curves $M(H)$.

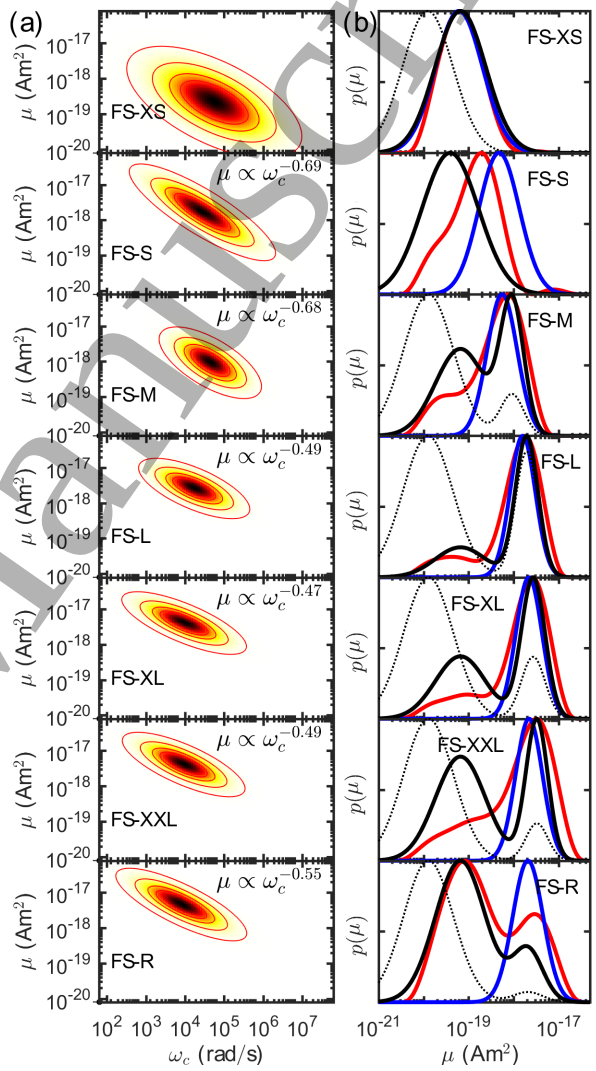

Figure A2. (a) Bivariate lognormal distribution obtained from fits to OM(H, ω) measurements. (b) Apparent magnetic moment distributions. The red curve is obtained by numerical inversion of the isothermal magnetization curves $M(H)$ and is weighted by the square of the magnetic moment. The black curve is the bimodal distribution obtained from analysis of high-field OM(H) measurements (the dotted line is weighted with the extinction properties of the particles; the solid line is the distribution weighted by the square of the moment). The blue curve is the moment distribution obtained from the bivariate analysis of the OM(H, ω) data in (a).

Table A1. Results from the Rietveld refinement of the XRD and ND room temperature data using the Fullprof Suite [24] with a cubic $Fd\bar{3}m$ space group for the iron oxide core phases [Fe tetrahedral site at (1/8, 1/8, 1/8); Fe Octahedral site at (1/2, 1/2, 1/2); O at (1/4, 1/4, 1/4)]. Below we show the list of parameters refined from neutrons, i.e., lattice parameters, weight fractions, average crystal size D_{cryst} of the cores, and Goodness of fit χ^2 and agreement factors R_{p}, R_{wp}, $R-\mathrm{Bragg}$.

		XRD			ND
		FS-XS	FS-R	FS-L	FS-L
Lattice parameters (Å)	iron oxide phase	$a = 8.360(1)$	$a = 8.359(1)$	$a = 8.351(1)$	$a = 8.357(1)$
		$a = 5.536(1)$	$a = 5.622(1)$	$a = 5.655(1)$	$a = 5.670(1)$
	β D-mannitol	$b = 8.669(1)$	$b = 8.697(1)$	$b = 8.671(1)$	$b = 8.816(1)$
		$c = 16.900(5)$	$c = 16.893(6)$	$c = 16.891(2)$	$c = 16.660(3)$
		$a = 4.906(1)$	$a = 4.913(1)$	$a = 4.912(1)$	$a = 4.912(1)$
	δ D-mannitol	$b = 18.240(3)$	$b = 18.252(2)$	$b = 18.245(2)$	$b = 18.251(3)$
		$c = 5.083(1)$	$c = 5.089(1)$	$c = 5.088(1)$	$c = 5.090(1)$
		$\beta = 118.19(1)$	$\beta = 118.25(1)$	$\beta = 118.34(1)$	$\beta = 118.29(1)$
	wüstite	–	–	–	$a = 4.286(1)$
Weight fraction (%)	iron oxide phase	43(1)	40(1)	34(1)	41(1)
	β D-mannitol	13(1)	8(1)	21(1)	3(1)
	δ D-mannitol	44(1)	52(1)	45(1)	54(1)
	wüstite	–	–	–	2(1)
D_{cryst} (nm)	iron oxide phase	7(2)	7(2)	11(4)	9(4)
χ^2		1.94	1.44	2.59	1.04
R_{p} (%)		6.05	6.35	7.93	0.928
R_{wp} (%)		7.75	8.09	1.2	1.17
$R-\mathrm{Bragg}$ (%)	iron oxide phase	12.4	5.64	7.81	4.41
	β D-mannitol	26.0	23.0	26.0	20.3
	δ D-mannitol	13.2	8.3	13.7	9.7
	wüstite	–	–	–	17.4

References

[1] Majetich S and Sachan M 2006 *J. Phys. D: Appl. Phys.* **39** R407

[2] Nie Z, Petukhova A and Kumacheva E 2010 *Nat. Nanotechnol.* **5** 15–25

[3] Eberbeck D, Wiekhorst F, Steinhoff U and Trahms L 2006 *J. Phys.: Condens. Matter* **18** S2829

[4] Zhou J, Leuschner C, Kumar C, Hormes J F and Soboyejo W O 2006 *Biomaterials* **27** 2001–2008

[5] Di Corato R, Espinosa A, Lartigue L, Tharaud M, Chat S, Pellegrino T, Ménager C, Gazeau F and Wilhelm C 2014 *Biomaterials* **35** 6400–6411

[6] Jordan A, Scholz R, Wust P, Fähling H and Felix R 1999 *J. Magn. Magn. Mater.* **201** 413–419

[7] Périgo E A, Hemery G, Sandre O, Ortega D, Garaio E, Plazaola F and Teran F J 2015 *Appl. Phys. Rev.* **2** 041302

[8] Rosensweig R E 2002 *J. Magn. Magn. Mater.* **252** 370–374

[9] Andreu I, Natividad E, Solozabal L and Roubeau O 2015 *ACS Nano* **9** 1408–1419

[10] Mehdaoui B, Tan R, Meffre A, Carrey J, Lachaize S, Chaudret B and Respaud M 2013 *Phys. Rev. B* **87** 174419

[11] Sadat M, Patel R, Sookoor J, Bud'ko S L, Ewing R C, Zhang J, Xu H, Wang Y, Pauletti G M, Mast D B *et al.* 2014 *Mater. Sci. Eng., C* **42** 52–63

[12] Blanco-Andujar C, Ortega D, Southern P, Pankhurst Q and Thanh N 2015 *Nanoscale* **7** 1768–1775

[13] Coral D F, Mendoza Zélis P, Marciello M, Morales M d P, Craievich A, Sánchez F H and Fernández van Raap M B 2016 *Langmuir* **32** 1201–1213

[14] Lartigue L, Hugounenq P, Alloyeau D, Clarke S P, Lévy M, Bacri J C, Bazzi R, Brougham D F, Wilhelm C and Gazeau F 2012 *ACS Nano* **6** 10935–10949

[15] Sakellari D, Brintakis K, Kostopoulou A, Myrovali E, Simeonidis K, Lappas A and Angelakeris M 2016 *Mater. Sci. Eng., C* **58** 187–193

[16] Hemery G, Genevois C, Couillaud F, Lacomme S, Gontier E, Ibarboure E, Lecommandoux S, Garanger E and Sandre O 2017 *Mol. Syst. Des. Eng.*

[17] Dutz S 2016 *IEEE Trans. Magn.* **52** 1–3

[18] Gavilán H, Kowalski A, Heinke D, Sugunan A, Sommertune J, Varón M, Bogart L K, Posth O, Zeng L, González-Alonso D, Balceris C, Fock J, Wetterskog E, Frandsen C, Gehrke N, Grüttner C, Fornara A, Ludwig F, Veintemillas-Verdaguer S, Johansson C and Morales M P 2017 *Part. Part. Syst. Charact.* **34** 1700094

[19] Gavilán H, Sánchez E H, Brollo M E, Asín L, Moerner K K, Frandsen C, Lázaro F J, Serna C J, Veintemillas-Verdaguer S, Morales M P and Gutiérrez L 2017 *ACS Omega* **2** 7172–7184

[20] Ludwig F, Wawrzik T, Yoshida T, Gehrke N, Briel A, Eberbeck D and Schilling M 2012 *IEEE Trans. Magn.* **48** 3780–3783

[21] Wetterskog E, Castro A, Zeng L, Petronis S, Heinke D, Olsson E, Nilsson L, Gehrke N and Svedlindh P 2017 *Nanoscale* **9** 4227–4235

[22] Hirt A M, Kumari M, Heinke D and Kraupner A 2017 *Molecules* **22** 2204

[23] Alba Venero D, Bender P, Espeso J, Fernández Barquín L, Fernández Díaz M T, González-Alonso D and Pankhurst Q 2015 *Institut Laue-Langevin (ILL)*

[24] Rodríguez-Carvajal J 1993 *Physica B: Condens. Matter* **192** 55–69

[25] Glatter O 1977 *J. Appl. Crystallogr.* **10** 415–421

[26] Hansen S 2000 *J. Appl. Crystallogr.* **33** 1415–1421

[27] Vestergaard B and Hansen S 2006 *J. Appl. Crystallogr.* **39** 797–804

[28] Bender P, Bogart L, Posth O, Szczerba W, Rogers S, Castro A, Nilsson L, Zeng L, Sugunan A, Sommertune J, Fornara A, González-Alonso D, Fernández Barquín L and Johansson C 2017 *Sci. Rep.* **7** 45990

[29] Glatter O 1979 *J. Appl. Crystallogr.* **12** 166–175

[30] Svergun D I and Koch M H 2003 *Rep. Prog. Phys.* **66** 1735

[31] Bender P, Balceris C, Ludwig F, Posth O, Bogart L, Szczerba W, Castro A, Nilsson L, Costo R, Gavilán H, González-Alonso D, de Pedro I, Fernández Barquín L and Johansson C 2017 *New J. Phys* **19** 073012

[32] Fock J, Jonasson C, Johansson C and Hansen M F 2017 *Phys. Chem. Chem. Phys.* **19**(13) 8802–8814

[33] Fock J, Balceris C, Costo R, Zeng L, Ludwig F and Hansen M F 2018 *Nanoscale* **10** 2052–2066 ISSN 2040-3364

[34] Ludwig F, Guillaume A, Schilling M, Frickel N and Schmidt A 2010 *J. Appl. Phys.* **108** 033918

[35] Bender P, Fock J, Frandsen C, Hansen M F, Balceris C, Ludwig F, Posth O, Wetterskog E, Bogart L K, Southern P, Szczerba W, Zeng L, Witte K, Grüttner C, Westphal F, Honecker D, González-Alonso D, Fernández Barquín L and Johansson C 2018 *J. Phys. Chem. C* **122** 3068–3077

[36] Wildeboer R, Southern P and Pankhurst Q 2014 *J. Phys. D: Appl. Phys.* **47** 495003

[37] Fronczek F R, Kamel H N and Slattery M 2003 *Acta Crystallogr., Sect. C: Cryst. Struct. Commun.* **59** o567–o570

[38] Shmakov A, Kryukova G, Tsybulya S, Chuvilin A and Solovyeva L 1995 *J. Appl. Crystallogr.* **28** 141–145

[39] Fock J, Bogart L K, González-Alonso D, Espeso J I, Hansen M F, Varón M, Frandsen C and Pankhurst Q A 2017 *J. Phys. D: Appl. Phys.* **50** 265005

[40] Okudera H, Kihara K and Matsumoto T 1996 *Acta Crystallogr., Sect. B: Struct. Sci.* **52** 450–457

[41] Battle P and Cheetham A 1979 *J. Phys. C: Solid State Phys.* **12** 337

[42] Shull C G, Strauser W and Wollan E 1951 *Phys. Rev.* **83** 333

[43] Coey J M D 2010 *Magnetism and Magnetic Materials* (Cambridge University Press) ISBN 9780521816144

[44] Krycka K L, Booth R A, Hogg C, Ijiri Y, Borchers J A, Chen W, Watson S, Laver M, Gentile T R, Dedon L R *et al.* 2010 *Phys. Rev. Lett.* **104** 207203

[45] Disch S, Wetterskog E, Hermann R P, Wiedenmann A, Vainio U, Salazar-Alvarez G, Bergström L and Brückel T 2012 *New J. Phys.* **14** 013025

[46] Negi D, Sharona H, Bhat U, Palchoudhury S, Gupta A and Datta R 2017 *Phys. Rev. B* **95** 174444

[47] Ahrentorp F, Astalan A, Blomgren J, Jonasson C, Wetterskog E, Svedlindh P, Lak A, Ludwig F, van IJzendoorn L J, Westphal F, Grüttner C, Gehrke N, Gustafsson S, Olsson E and Johansson C 2015 *J. Magn. Magn. Mater.* **380** 221–226

[48] Kallumadil M, Tada M, Nakagawa T, Abe M, Southern P and Pankhurst Q A 2009 *J. Magn. Magn. Mater.* **321** 1509–1513